Available online at www.sciencedirect.com
SCIENCE DIRECT®
International Journal of Heat and Mass Transfer 47 (2004) 5665–5683
International Journal of HEAT and MASS TRANSFER
www.elsevier.com/locate/ijhmt

Computation of flow and heat transfer in rotating two-pass rectangular channels (AR = 1:1, 1:2, and 1:4) with smooth walls by a Reynolds stress turbulence model

Guoguang Su [a], Hamn-Ching Chen [b], Je-Chin Han [a,*], James D. Heidmann [c]

[a] *Turbine Heat Transfer Laboratory, Department of Mechanical Engineering, Texas A&M University, College Station, Texas 77843-3123, USA*
[b] *Ocean Engineering Program, Department of Civil Engineering, Texas A&M University, College Station, Texas 77843, USA*
[c] *NASA Glenn Research Center, 21000 Brookpark Road, MS 5-11, Cleveland, OH 44135, USA*

Received 24 October 2003; received in revised form 9 July 2004
Available online 16 September 2004

Abstract

Numerical predictions of three-dimensional flow and heat transfer are presented for rotating two-pass smooth channels with three aspect ratios (AR = 1:1; 1:2; 1:4). Detailed predictions of mean velocity, mean temperature and Nusselt number for two Reynolds numbers (Re = 10,000 and 100,000) were carried out. A total of fifteen calculations have been performed with various combinations of rotation number, Reynolds number, and coolant-to-wall density ratio. The rotation number and inlet coolant-to-wall density ratio varied from 0.0 to 0.28 and from 0.13 to 0.40, respectively. The focus of this study is to investigate the effect of the channel aspect ratio, the Reynolds number, and the coolant-to-wall density ratio on the nature of the flow and heat transfer. A multi-block Reynolds-averaged Navier–Stokes (RANS) method was employed in conjunction with a near-wall second-moment turbulence closure. In the present method, the convective transport equations for momentum, energy, and turbulence quantities are solved in curvilinear, body-fitted coordinates using the finite-analytic method.

1. Introduction

Increased turbine inlet temperature is a guarantee of high thermodynamic efficiency of gas turbines. However, the melting point of the metals used for turbine components restricts the unbounded increase of gas temperature. This dilemma is compromised by a cooling technique in which a few percent of the mainstream air is diverted from various points in the compression process and passed through the blades and the other components. Cooling of the components is therefore essential for gas turbine performance and life, which are crucially affected by the design of the coolant supply system. Typically the coolant flows through a series of straight ducts connected by 180° turns and roughened with ribs or pin fins. These cooling ducts may not only be square in cross-section; the aerodynamic shape of the turbine blade dictates the use of cooling channels that are rectangular in cross-section (with different aspect ratios). The investigation of the flow and heat transfer in these ducts is especially important for the design of the

* Corresponding author. Tel.: +1 979 845 3738; fax: +1 979 862 2418.
E-mail address: jchan@mengr.tamu.edu (J.-C. Han).

0017-9310/$ - see front matter © 2004 Elsevier Ltd. All rights reserved.
doi:10.1016/j.ijheatmasstransfer.2004.07.019

Nomenclature

AR	channel aspect ratio	Ro	rotation number, $\Omega D_h/W_b$
D_h, D	hydraulic diameter	R_r	radius from axis of rotation
h	heat transfer coefficient	S	streamwise distance
k	thermal conductivity of coolant	T	local coolant temperature
L	total length of the channel	T_0	coolant temperature at inlet
L_1	unheated smooth starting section of the channel	T_w	local wall temperature
		W_b	bulk velocity in streamwise direction
L_2	heated section of the channel	ρ	density of coolant
L_3	unheated smooth exit section of the channel	$\Delta\rho/\rho$	inlet coolant-to-wall density ratio, $(T_w - T_0)/T_w$
Nu	local Nusselt number, hD/k		
Nu_0	Nusselt number in fully-developed turbulent non-rotating tube ($Nu_0 = 0.023Re^{0.8}Pr^{0.4}$)	Ω	rotational speed
		θ	dimensionless temperature, $(T - T_0)/(T_w - T_0)$
Pr	Prandtl number		
Re	Reynolds number, $\rho W_b D_h/\mu$	μ	dynamic viscosity of coolant

cooling passage. It is the intention of this study to facilitate a comprehensive understanding of the characteristics of flow and heat transfer in these ducts through numerical prediction.

It is understood that the flow in a rotating duct with bend is dominated by the Coriolis force, centrifugal buoyancy force, and pressure gradient induced by the curvature of the bend; a successful prediction of such channels must capture these effects. Several numerical predictions were performed by Prakash and Zerkle [1], Bo et al. [2], Besserman and Tanrikut [3], Sathyamurthy et al. [4], McGrath and Tse [5], and Hwang et al. [6]. Basically, they employed the k–ε model in their simulation of the stationary or rotating square duct. Their studies showed that: The k–ε/one-equation EVM produces reasonable heat transfer predictions, but some deficiencies emerge at the higher rotation numbers. The low-Re k–ε EVM predictions showed unrealistic behavior, while the low-Re ASM results for stationary duct are close to the Wagner et al. [7] measurements. They suggested that a low Reynolds number turbulence model is necessary to simulate real gas turbine engine conditions and a Reynolds stress model is required to capture anisotropic effects.

Iacovides et al. [8] explored turbulence modeling issues related to duct flow influenced by strong curvature (180° bend) and rotation. Compared with their detailed experimental data [9], they suggested that the refinement of modeling being based on the low-Re (rather than algebraic) second-moment closure looks promising. Bonhoff et al. [10] presented the heat transfer predictions for rotating U-shaped coolant channels. The differential Reynolds stress model (RSM) in the FLUENT code was used for the calculation. The averaged heat transfer predictions were close to the Wagner et al. [7] experimental results in the first passage of the channel, while the heat transfer in the second passage was overestimated by RSM, he concluded that the differential stress model thermal computations were clearly superior to those of the k–ε/one-equation model. Stephens et al. [11] and Stephens and Shih [12] predicted the nature of the three-dimensional flow induced by Coriolis force, centrifugal buoyancy and a 180° bend in a rotating two-pass square duct with smooth walls. The computations were performed using a low Reynolds number k-ω model of turbulence and the computed heat transfer coefficient compared reasonably well with Wagner et al. [7] experimental data.

Lin et al. [13] used a shear-stress transport (SST) turbulence model in the investigation of heat transfer in a rotating two-passage square duct. They studied the effects of Reynolds numbers, rotation numbers, and buoyancy parameters. Chen et al. [14,15] employed a multi-block numerical method for the calculation of three-dimensional flow and heat transfer in rotating two-pass square channels (AR = 1:1) with smooth walls. Their comparison of second-moment and two-layer calculations with experimental data clearly demonstrated that the secondary flows in rotating two-pass channels were strongly influenced by the Reynolds stress anisotropy resulting from the Coriolis and centrifugal buoyancy forces as well as the 180° wall curvatures. The near-wall second-moment closure model provided accurate heat transfer predictions which agree well with Wagner et al. [7] measured data. Using the same model, Jang et al. [16,17] studied flow and heat transfer behavior in a non-rotating two-pass square channel with 60° and 90° ribs. Their results were in good agreement with Ekkad and Han's [18] detailed heat transfer data and demonstrated the second-moment closure model superiority in predicting flow and heat transfer characteristics in the ribbed duct. In a later study, Jang et al. [19]

predicted flow and heat transfer in a rotating square channel with 45° angled ribs by the same second-moment closure model. Heat transfer coefficient prediction was well matched with Johnson et al. [20] data for both stationary and rotating cases. This has affirmed the superiority of the second-moment closure model compared to simpler isotropic eddy viscosity turbulence models. More recently, Al-Qahtani et al. [21] predicted flow and heat transfer in rotating two-pass rectangular channels (AR = 2:1) with 45° rib turbulators and Su et al. [22] predicted flow and heat transfer in rotating rectangular channels (AR = 4:1) with V-shaped ribs. Their numerical results were also in agreement with Azad et al. [23] experiment data and Lee et al. [24] measurements, respectively. These results further demonstrated the capability of the second-moment closure model for accurate prediction of sophisticated cooling channel configurations.

The previous research focused on the validation of turbulence models and the physical behavior of the flow and heat transfer in the square duct (AR = 1:1) or channels with aspect ratios greater than one (AR = 2:1, and 4:1). However, confined by the blade configurations, the cooling passage should include not only these higher aspect ratio ducts, but also the lower aspect ratio ducts, such as the AR = 1:2 and 1:4 channels considered in the present study. The heat transfer and flow behavior in these lower aspect ratio ducts has not yet been investigated. This paper focuses on the prediction of three-dimensional flow and heat transfer for several rotating and non-rotating two-pass rectangular smooth ducts (AR = 1:1, 1:2, and 1:4) using the second moment RANS method of Chen et al. [14,15]. The numerical results are compared with the experimental data of Fu et al. [25] for both the stationary and rotating AR = 1:4 rectangular channels. In addition, the effects of high Reynolds number, high rotation, and high density ratios on heat transfer coefficients and friction factors are also investigated.

2. Description of problem

A schematic diagram of the geometry for AR = 1:4 duct is shown in Fig. 1. As mentioned earlier, this investigation covers three channels with different aspect ratios (AR = 1:1, 1:2 and 1:4). For the sake of brevity, however, only the geometry for the AR = 1:4 channel is given in Fig. 1. All three ducts have the same length, same bend radius, and the same width between the inner and outer wall. Of the four side walls, the two in the rotational direction are denoted as leading and trailing surfaces, while the other two are denoted as inner and outer surfaces. The total length of the channel, L, equals to 37.47 cm (14.75 in.), the distance from the inlet of the channel to the axis of rotation is given by $R_r = 40.64$ cm (16 in.). The channel consists of an unheated smooth starting section ($L_1 = 22.23$ cm (8.75 in.)) and a heated section ($L_2 = 15.24$ cm (6 in.)). The radius of curvature of the 180° sharp turn is $r_i = 0.635$ cm (0.25 in.) and the minimum gap G between the inner and outer surfaces of the bend is 1.27 cm (0.5 in.). The channel width W is kept the same at 1.27 cm (0.5 in.) for all three different aspect ratio channels. The channel height is increased from 1.27 cm (0.5 in.) for square duct to 5.08 cm (2.0 in.) for AR = W/H = 1:4 channel. It should be noted that the hydraulic diameters D_h are different for different aspect ratio channels with $D_h = 1.27$ cm, 1.69 cm, and 2.03 cm for AR = 1:1, 2:1, and 4:1 channels, respectively. For the rotating cases, the channel orientations is given as $\beta = 90°$. A summary of all fifteen (15) cases studied is given in Table 1. Because the hydraulic radius are different for different aspect ratio ducts, it is necessary to adjust the channel inlet velocity and rotating speed in order to maintain the same Reynolds number and the same rotation number in the present numerical simulations.

3. Computational procedure

3.1. Overview

The Reynolds-averaged Navier–Stokes (RANS) equations in conjunction with a near-wall Reynolds stress turbulence model are solved using the chimera RANS method of Chen et al. [14,15]. The governing equations with the second-moment closure turbulence model were described in detail in Chen et al. [14,15] and will not be repeated here. The flow is considered to be incompressible since the Mach number is quite low. However, the density in the centrifugal force terms is approximated by $\rho = \rho_0 T_0/T$ to account for the density variations caused by the temperature differences. Where ρ_0 and T_0 are the density and temperature at the inlet of the cooling channel. In general, the density is also a function of the rotating speed because the centrifugal force creates a pressure gradient along the duct. The corresponding experiment condition gives a maximum density variation of only about 1.1% from the inlet to the exit of the duct at the highest rotation number. It is therefore reasonable to omit the density variation caused by the pressure gradients induced by the channel rotation.

3.2. Boundary conditions

A uniform velocity profile was used at the inlet of the duct ($Z = 0$). The unheated length (L_1) was of sufficient length for the coolant to reach the fully developed turbulent velocity profile before entering the heated section ($Z = L_1$). At the exit of the duct, zero-gradient boundary conditions were specified for the mean velocity and all

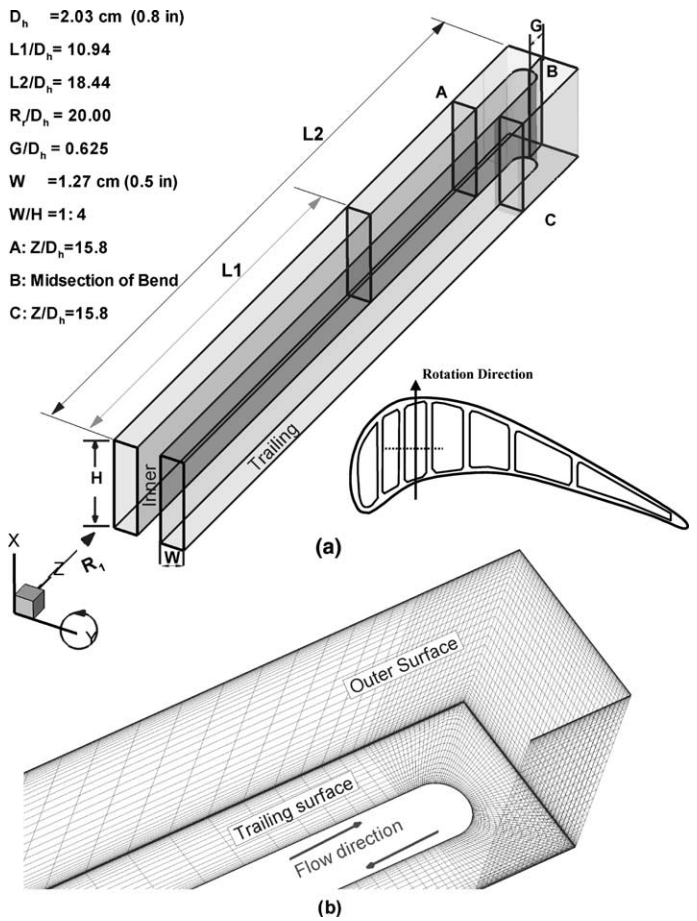

Fig. 1. Geometry, conceptual view of rotating channel orientation and numerical grid for rectangular duct (AR = 1:4).

Table 1
Summary of cases studied

Case #	AR	β (°)	Re	Ro	$\Delta\rho/\rho$
Case 1	1:1	–	10,000	0.0	0.13
Case 2	1:1	90	10,000	0.14	0.13
Case 3	1:2	–	10,000	0.0	0.13
Case 4	1:2	90	10,000	0.14	0.13
Case 5	1:4	–	10,000	0.0.0	0.13
Case 6	1:4	90	10,000	0.14	0.13
Case 7	1:1	–	100,000	0.0	0.13
Case 8	1:1	90	100,000	0.28	0.20
Case 9	1:2	–	100,000	0.0	0.13
Case 10	1:2	90	100,000	0.28	0.20
Case 11	1:4	–	100,000	0.0.0	0.13
Case 12	1:4	90	100,000	0.28	0.20
Case 13	1:1	90	100,000	0.28	0.40
Case 14	1:2	90	100,000	0.28	0.40
Case 15	1:4	90	100,000	0.28	0.40

turbulent quantities, while linear extrapolation was used for the pressure field. The coolant fluid at the inlet of the duct is air at uniform temperature $T = T_0$ (i.e., $\theta = (T - T_0)/(T_w - T_0) = 0$). The wall temperature of

the unheated sections is kept constant at $T = T_0$ ($\theta = 0$) while the wall temperature of the heated section is kept constant at $T = T_w$ ($\theta = 1$).

3.3. Computational grid details

Fig. 1(b) shows the computational grid for the smooth rectangular duct with AR = 1:4. For the sake of brevity, the numerical grids for AR = 1:1 and 1:2 channel are not included here. In order to provide adequate resolutions of the viscous sub-layer and buffer layer adjacent to a solid surface, the minimum grid spacing for the Re = 10,000 cases is maintained at 10^{-4} of the hydraulic diameter which corresponds to a wall coordinate y^+ of the order of 0.1. A systematic grid refinement study was performed for all three different aspect ratio ducts. The grid refinement in the axial direction at the bend region has produced only minor changes of Nusselt number ratio. The refinement of cross-sectional grids resulted in a maximum improvement of 3.5% in Nusselt number ratios when the grid number increase about 50%. The minimum grid spacing for the Re = 100,000 cases is maintained at 2×10^{-5} of the hydraulic diameter which corresponds to wall coordinate y^+ on the order of 0.1 also. The refinement in the axial direction at the bend region produced only minor changes of Nusselt number ratio, while the refinement of cross-sectional grids caused a maximum of 4.1% improvement at the bend region in Nusselt number ratios when the grid number increase about 50%. In all calculations, the root-mean-square (rms) and maximum absolute errors for both the mean flow and turbulence quantities were monitored for each computational block to ensure complete convergence of the numerical solutions and a convergence criterion of 10^{-5} was used for the maximum rms error.

4. Results and discussion

This section presents the three-dimensional mean flow, the temperature field, the Nusselt number ratios,

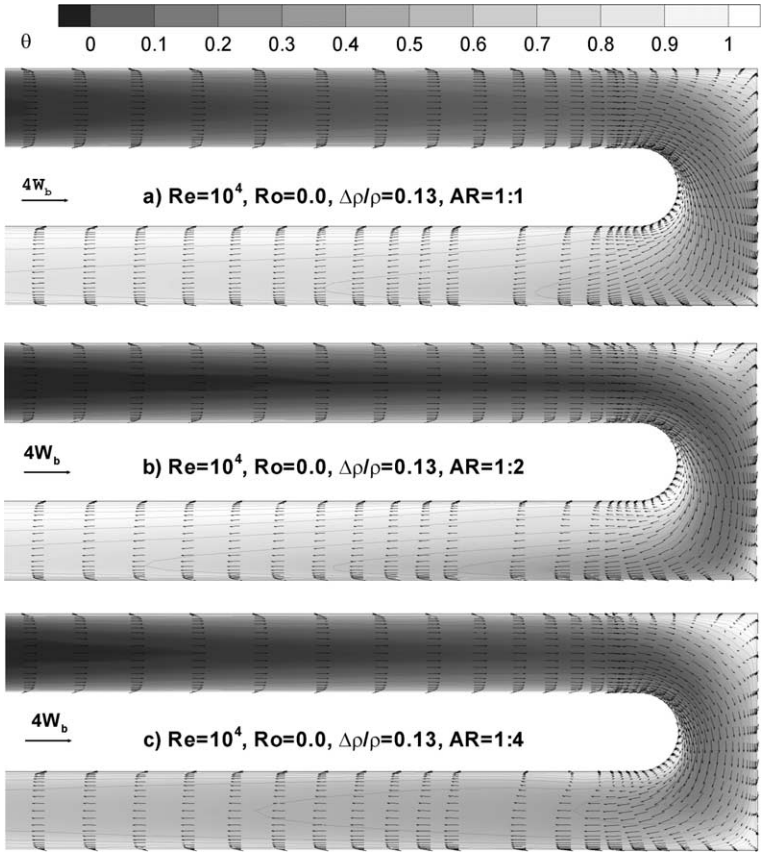

Fig. 2. Velocity vectors and dimensionless temperature [$\theta = (T - T_i)/(T_w - T_i)$] contour on the middle plane of non-rotating ducts (Re = 10,000, Ro = 0.0, $\Delta\rho/\rho$ = 0.13) (Cases 1, 3 and 5).

and the friction factor ratios for the ducts with three different aspect ratios of AR = 1:1, 1:2, and 1:4, respectively.

4.1. Velocity and temperature fields

Fig. 2 shows the dimensionless temperature contour (θ) and the velocity vector field in the heated section at the middle plane between the leading and trailing surfaces for all three non-rotating ducts. It is noted that the flow patterns are similar in the first pass before the bend. The flow separations occur almost at the same location since the band radius is the same for all three ducts and the flow is fully developed before reaching the bend. On the other hand, the heat transfer characteristics are significantly different in the second pass because the secondary flows induced by the bend are drastically different for different aspect ratio channels. It can be seen that the high-momentum fluid entering the turn from the inflow passage impinges on the outer wall. As the flow turns into the second passage, the high-momentum flow again impinges on the outer wall. These flow impingements produced two distinct high heat transfer enhancement regions along the outer wall which will be discussed in detail in the next section.

Fig. 3 shows the dimensionless temperature contour (θ) and the vector field for Re = 10,000 cases at three axial Stations (A) (Z/D_h = 15.8), (B) (midsection of the bend), and C (Z/D_h = 15.8) as denoted in Fig. 1. Moreover, the Nusselt number ratios on all four walls are also shown in Fig. 3 to facilitate a detailed understanding of the heat transfer characteristics in different aspect ratio channels. Note that the Nusselt numbers presented here

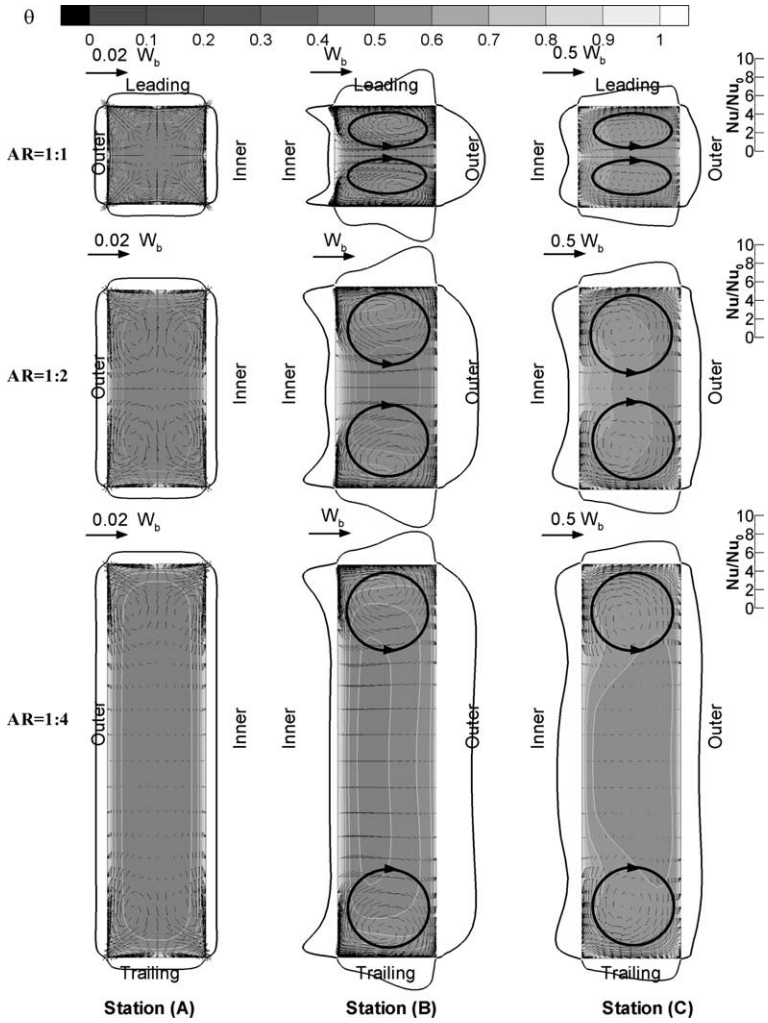

Fig. 3. Secondary flow, dimensionless temperature [$\theta = (T - T_i)/(T_w - T_i)$] contours, and Nusselt number ratios for non-rotating ducts (Re = 10,000, Ro = 0.0, $\Delta\rho/\rho$=0.13) (Cases 1, 3 and 5).

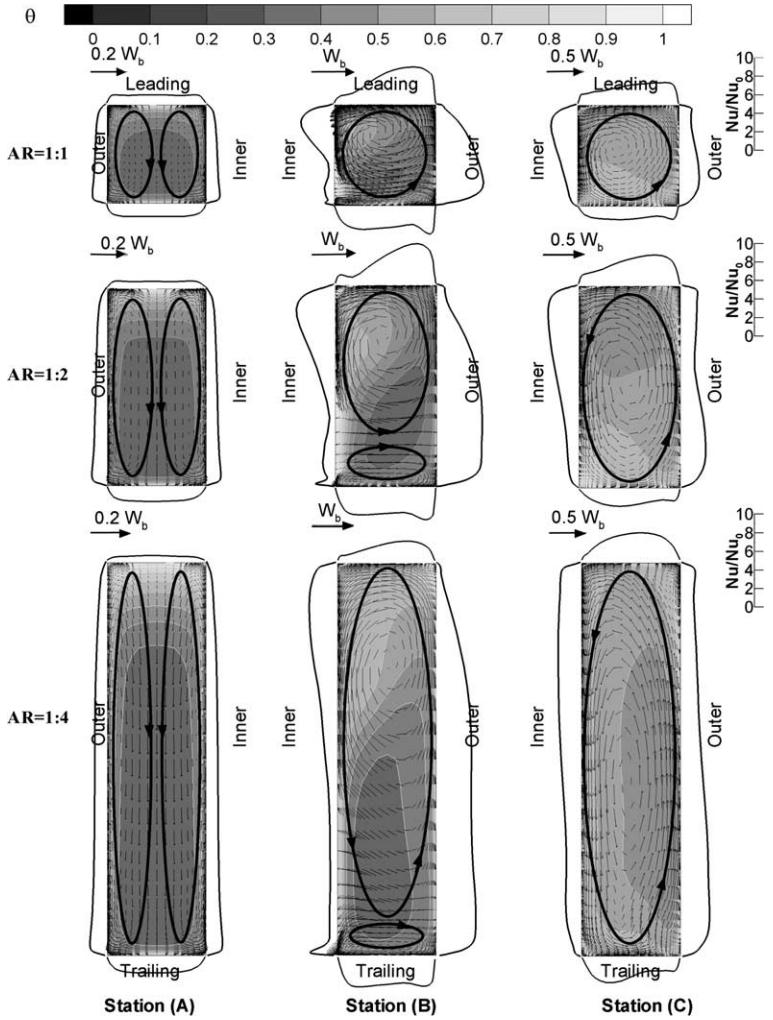

Fig. 4. Secondary flow, dimensionless temperature $[\theta = (T - T_i)/(T_w - T_i)]$ contours, and Nusselt number ratios for rotating ducts (Re = 10,000, Ro = 0.14, $\Delta\rho/\rho$=0.13) (Cases 2, 4 and 6).

are normalized by the smooth tube correlation of Dittus–Boelter.

For the three non-rotating ducts, it is seen from that the anisotropy of the turbulent Reynolds stresses produced eight small secondary corner vortices in the first passage for all three channels. These vortices grow in the vertical direction as the channel aspect height was increased from AR = 1:1 to 1:2. However, the vortices cease to expand in the vertical direction when the channel height was further increased to AR = 1:4. It should be noted that these Reynolds-stresses-driven vortices are rather weak and did not significantly alter the Nusselt number ratios along the channel surfaces. As the fluid flows through the 180° bend, the centrifugal forces arising from the curvature and the associated pressure gradients (low pressure at inner surface, high pressure at outer surface) produced a pair of counter-rotating vortices in the bend. These vortices are significantly stronger than those vortices observed in the first passage and are responsible for the transport of cool fluid from the core toward the outer surface. Before the bend, the cooler fluid is located in the core region. After the bend, however, the cooler fluid is pushed toward the outer surface by the centrifugal force induced by the streamline curvatures. This leads to steeper temperature gradients on the outer wall than on the inner wall after the bend as shown in Station (C) of Fig. 3.

It is further noted in Fig. 3 that there are distinct differences in the secondary flow patterns for different aspect ratio ducts. For the square duct, the counter-rotating vortex pair generated by the bend is squashed in the vertical direction due to the tight spacing between the leading and trailing surfaces. In the low aspect ratio rectangular ducts, however, the vortices induced by the

180° turn tend to maintain circular shapes up to the space limitations rather than expanding continuous in the vertical direction. In the AR = 1:1 and 1:2 channels, the counter-rotating vortices occupy the entire channel and bring cooler fluid in the core region towards the outer surface at both Stations (B) and (C). For the AR = 1:4 channel, however, the nearly circular vortex pair are confined to the leading and trailing surfaces. Even though the secondary flow is very weak in the middle section of the AR = 1:4 channel, the additional pressure gradients induced by the counter-rotating vortices still apply over the entire channel cross-section. Consequently, the cooler fluid in the middle section of the AR = 1:4 channel was pushed by the vortex-induced pressure gradients back towards the inner surface as seen in Station (B).

Fig. 4 shows the cross-stream velocity vectors and the temperature contours for the Re = 10,000 rotating ducts at the same location as those presented in Fig. 3. It is quite clear that the flow patterns in both the first and second passages were significantly modified by the rotation-induced vortices. In the first passage, the Coriolis forces produce a pair of counter-rotating vortices which moves cooler fluids in the core region toward the trailing surface of the rotating ducts. In the second passage, the Coriolis force acts in the opposite direction, which pushes the cold fluid toward the leading surface. In the bend, the vortex pair formed in the first passage by channel rotation is overpowered by the bend-induced vortices. The combined effects of the rotation- and turn-induced vortices increases the strength and size of the vortex near the leading surface as seen in Fig. 4(B). In the second passage, the

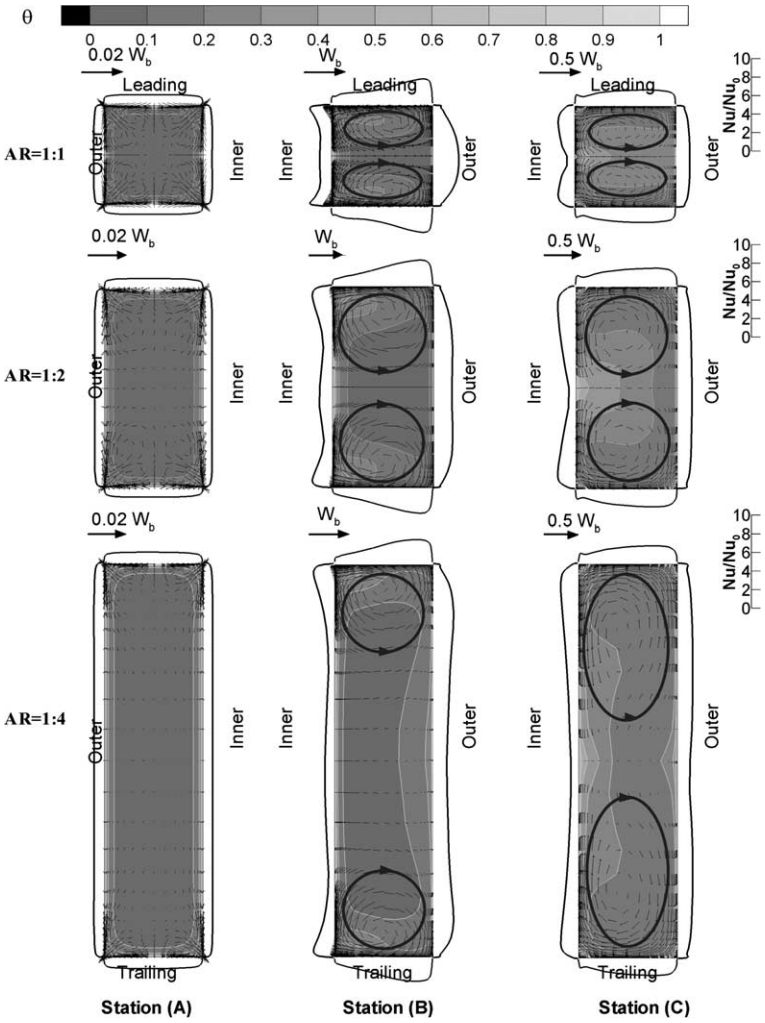

Fig. 5. Secondary flow, dimensionless temperature [$\theta = (T - T_i)/(T_w - T_i)$] contours and Nusselt number ratios for non-rotating ducts (Re = 100,000, Ro = 0.0, $\Delta\rho/\rho$=0.13) (Cases 7, 9 and 11).

larger vortex near the leading surface continued to grow and eventually occupied almost the entire space. This flow pattern is further modified by the centrifugal buoyancy force which plays an opposite role in the second passage as it does in the first passage. The combination of these forces influences the heat transfer characteristics which will be presented in the next section.

Fig. 5 shows the velocity vectors and temperature contours for non-rotating ducts for the high Reynolds number (Re = 100,000) cases. Comparing Fig. 5 with 3 for non-rotating ducts, the thermal boundary layers become thinner at higher as the Reynolds number increases. The overall secondary flow patterns are quite similar between the low and high Reynolds number cases, but the bend-induced vortices are somewhat stronger at Re = 100,000. For the AR = 1:1 and 1:2 channels, the cooler fluids at section (B) were pushed toward the outer surface by the centrifugal force and the bend-induced vortices which occupy the entire channel cross-section. For the AR = 1:4 channel, however, the counter-rotating vortices were again confined to the leading and trailing surfaces and the cooler fluid in themiddle section was pushed toward the inner surface by the vortex-induced pressure gradients.

Fig. 6 shows the effects of high Reynolds number (Re = 100,000) and high rotation number (Ro = 0.28) on the temperature contours and secondary flow vectors. Comparing to the low-Re and low-Ro cases shown in Fig. 4, it is clearly seen that the rotation-induced vortices become stronger when both the Reynolds number and rotation number were increased. In the bend region, however, the vortices induced by the turn were also

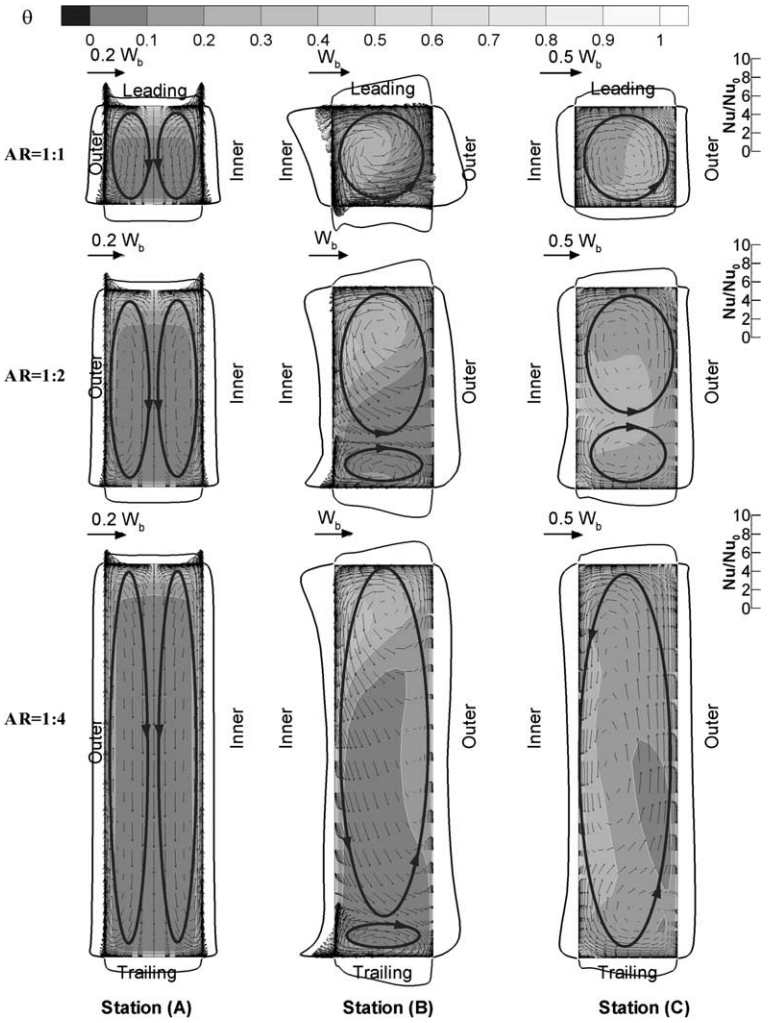

Fig. 6. Secondary flow, dimensionless temperature $[\theta = (T - T_i)/(T_w - T_i)]$ contours and Nusselt number ratios for rotating ducts (Re = 100,000, Ro = 0.28, $\Delta\rho/\rho$ = 0.20) (Cases 8, 10 and 12).

strengthened as the Reynolds number was increased from $Re = 10{,}000$ to 100,000. It is noted that the rotation-induced vortices are still relatively weak in comparison with the bend-induced vortices (see Fig. 5) even though the rotation number was doubled from 0.14 to 0.28. In the second passage, the vortex adjacent to the leading surface grows considerably but the vortex next to the trailing surface remains clearly visible. This suggests that the rotation effect is not strong enough to suppress the bend-induced vortices completely in these high Reynolds number rotating ducts.

4.2. Heat transfer coefficient and friction factor distribution

The Nusselt numbers presented here are normalized by the smooth tube correlation by Dittus–Boelter for fully developed, turbulent, non-rotating, tube flow was defined earlier. Similarly, the friction factors are also normalized by the following smooth tube correlation:

$$C_{f0} = 0.078Re^{-0.25} \tag{1}$$

4.3. Effect of channel aspect ratio and rotation on heat transfer coefficient distribution

Fig. 7 shows the Nu/Nu_0 contour plots on the leading and trailing surfaces of all three channels with different aspect ratios for the rotating and non-rotating cases. For the non-rotating ducts (Cases 1, 3 and 5), three common features are observed in both the square and rectangular channels: (1) In the first passage, the Nusselt number ratio is high near the inlet due to the thin thermal boundary layers; (2) The heat transfer in the bend is high due to the secondary flows induced by the centrifugal forces and the associated pressure gradients. Especially, at the middle part of bend, the heat transfer is high due to the combined effects of flow impingement and bend-induced vortices. Near the end of the bend, the mainstream flow again impinges on the outer wall and produces another high heat transfer region after the second sharp corner; (3) Downstream in the second passage, the heat transfer coefficient decreases and asymptotically approaches the fully developed value. It is noted that the difference of Nusselt number ratios

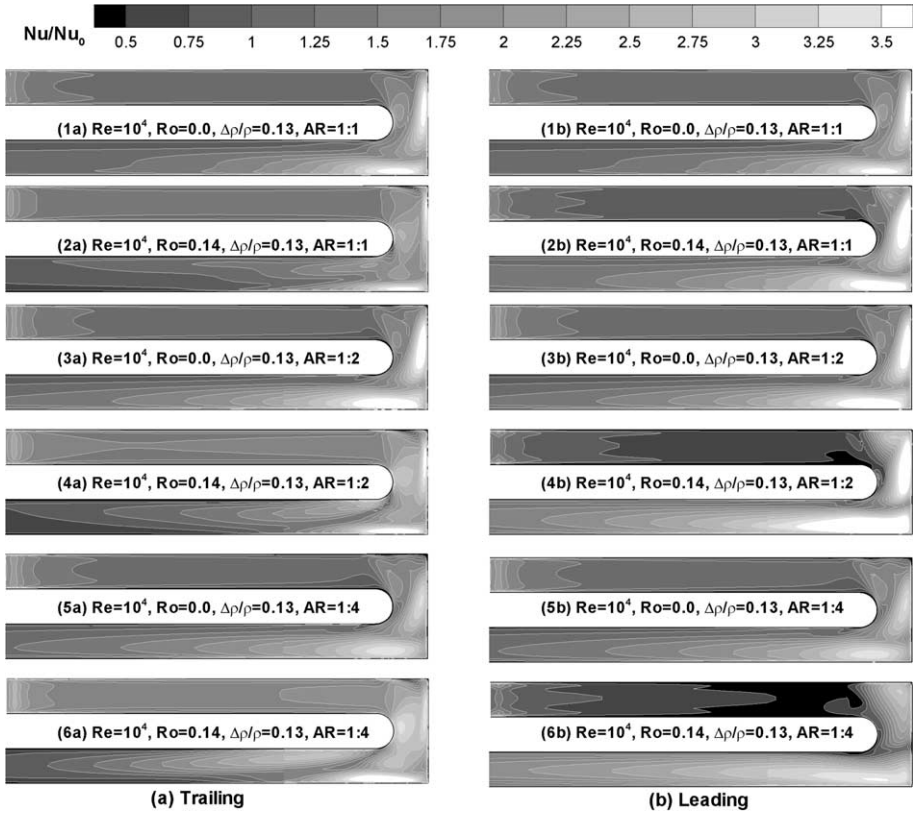

Fig. 7. Nusselt number ratio contours on (a) trailing and (b) leading surface for lower Reynolds number cases ($Re = 10{,}000$; Cases 1–6).

among the three non-rotating ducts are not widely different, except in the bend.

For the rotating ducts (Cases 2, 4 and 6), the following common heat transfer characteristics are also observed in all three channels: (1) In the first passage, the Nusselt number ratio on the trailing surface is higher than that on the leading surface. In contrast, in the second passage, the Nusselt number ratio on the leading surface is higher than that on the trailing surface. This agrees well with the analysis of the flow and temperature fields; (2) On the leading surface, the Nusselt number ratio reaches minimum in the middle of the first passage and increases significantly in the bend. In the second passage, the Nusselt number ratio reaches a higher level than that on the same location in non-rotating ducts. For the trailing surface, the Nusselt number ratio increases sharply in the streamwise direction compared with the non-rotating counterpart and reaches a maximum value in the bend region. In the second passage, the Nusselt number ratio decreases gradually along the duct.

In general, the observed differences in the Nusselt number ratios among the rotating ducts is more pronounced than those among the non-rotating ducts. This clearly indicated that the channel aspect ratio has a more significant effect on the Nusselt number ratios in rotating ducts although this effect is still small. This can be attributed to the differences in the secondary flow pattern for different aspect ratio ducts.

Fig. 8 presents the spanwise-averaged Nusselt number ratios for both the non-rotating Case 5 and the rotating Case 6. Regional averaged (averaged spanwise and over certain S/D_h values) Nusselt number ratios are compared to the experimental data obtained by Fu et al. [25] for the same cases to validate the numerical results in this study. It is seen that the numerical predictions are in agreement with the experimental data except in the bend region. This discrepancy may be due to the fact that the flow conditions and thermal boundary conditions in the measurement are not completely consistent with the idealized condition in numerical prediction.

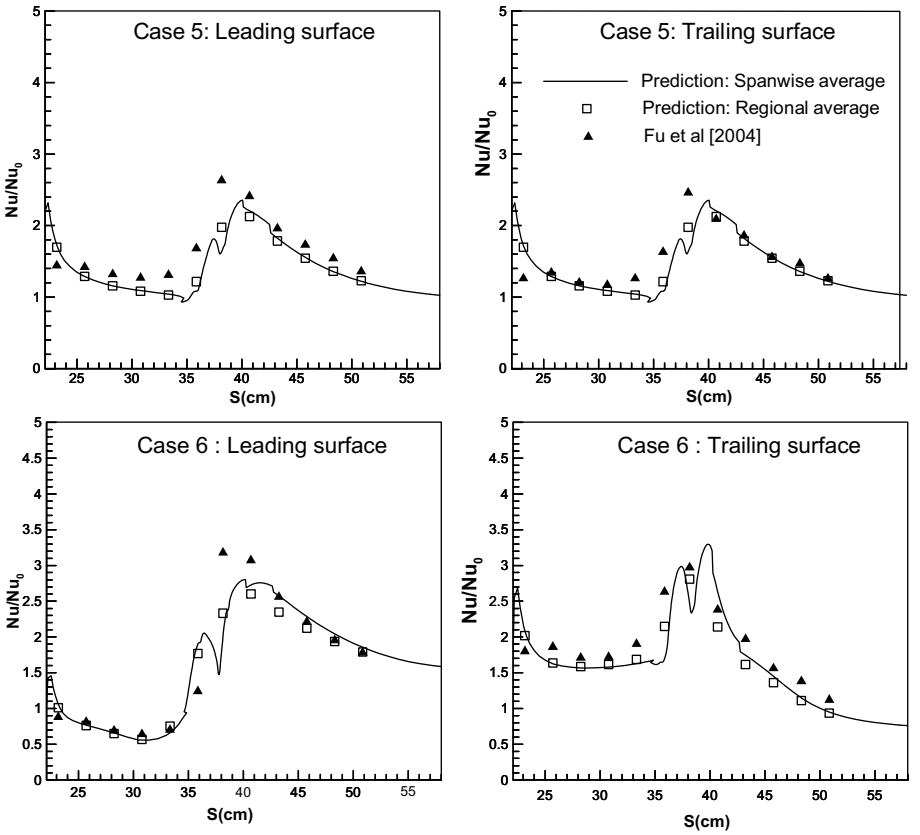

Fig. 8. Comparison between calculated and measured Nusselt number ratios for non-rotating (Case 5) and rotating (Case 6: $Ro = 0.14$) ducts ($Re = 10{,}000$, $\Delta\rho/\rho = 0.13$, AR = 1:4).

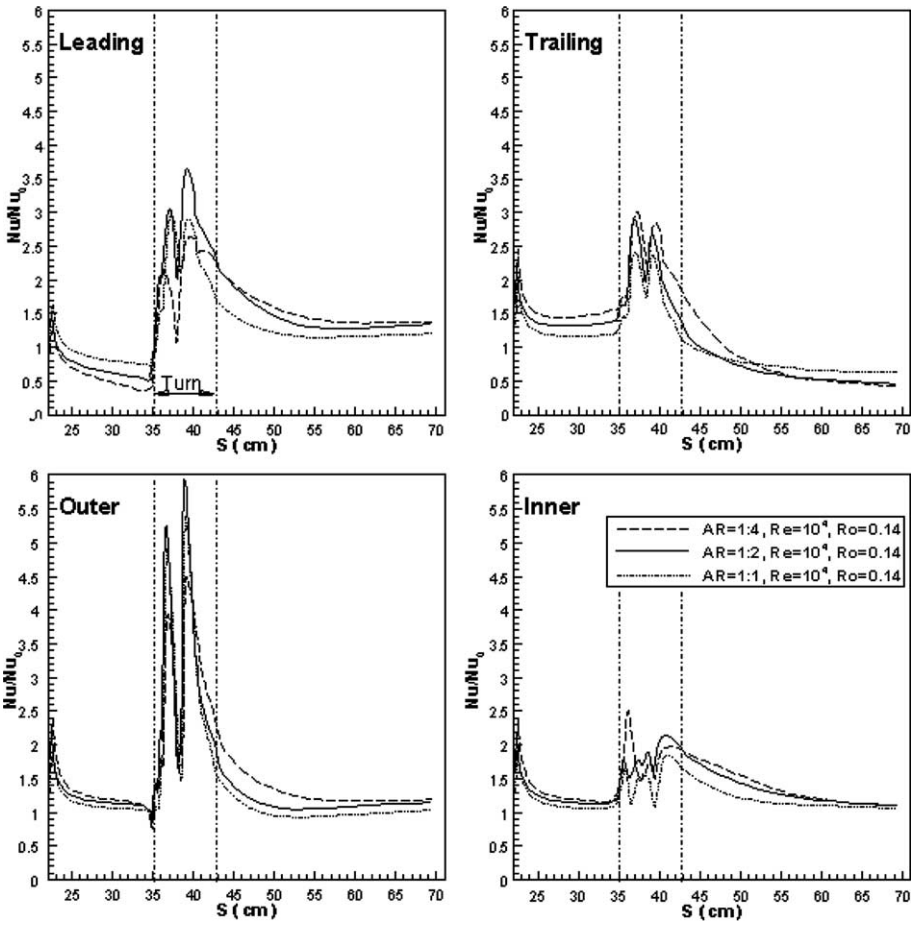

Fig. 9. Effect of channel aspect ratio on spanwise-averaged Nusselt number ratios for lower Reynolds number rotating duct ($Ro = 0.14$, $Re = 10{,}000$, $\Delta\rho/\rho = 0.13$) (Cases 2, 4 and 6).

Fig. 9 presents the spanwise-averaged Nusselt number ratios for the rotating ducts (Cases 2, 4 and 6). Referring to the detailed Nusselt number ratio contours (Fig. 7), one can see that the spanwise-average Nusselt num0ber ratios on the trailing surface of the first passage and on the leading surface of the second passage were increased by rotation. It is quite clear that the effects of channel aspect ratio become more pronounced under rotating conditions. In the first passage, the Coriolis force pushes colder fluid towards the trailing surface and the rotation-induced vortices brings hotter fluid back to the leading surface. The rotation-induced vortices becomes stronger when the channel aspect ratio is reduced from AR = 1:1 to 1:4. Consequently, the Nusselt number increases on the trailing surface and reduces on the leading surfaces as the channel aspect ratio reduces. This trend is reversed in the second passage since the Coriolis force acts in the opposite direction after the bend. In the bend region, the Nusselt number ratio on all four surfaces of the AR = 1:2 duct is higher than those observed in the square duct. As the channel aspect ratio was reduced further to AR = 1:4, however, the Nusselt number ratios on the leading and outer surfaces drop sharply since the heat transfer enhancement due to the bend-induced vortices are confined to the leading and trailing surfaces for low aspect ratio ducts.

4.4. Effect of high Reynolds number on heat transfer coefficient distribution

In addition to the non-rotating and rotating ducts with a relatively low Reynolds number presented above (Cases 1–6), calculations were also performed for high Reynolds number, high density ratio, and high rotation number cases (i.e., Cases 7–15) which are closer to power-generation turbine blade cooling conditions. In these calculations, the Reynolds number is increased from 10^4 to 10^5; the rotation number is doubled from 0.14 to 0.28; and the density ratio is increased from 0.13 to 0.4.

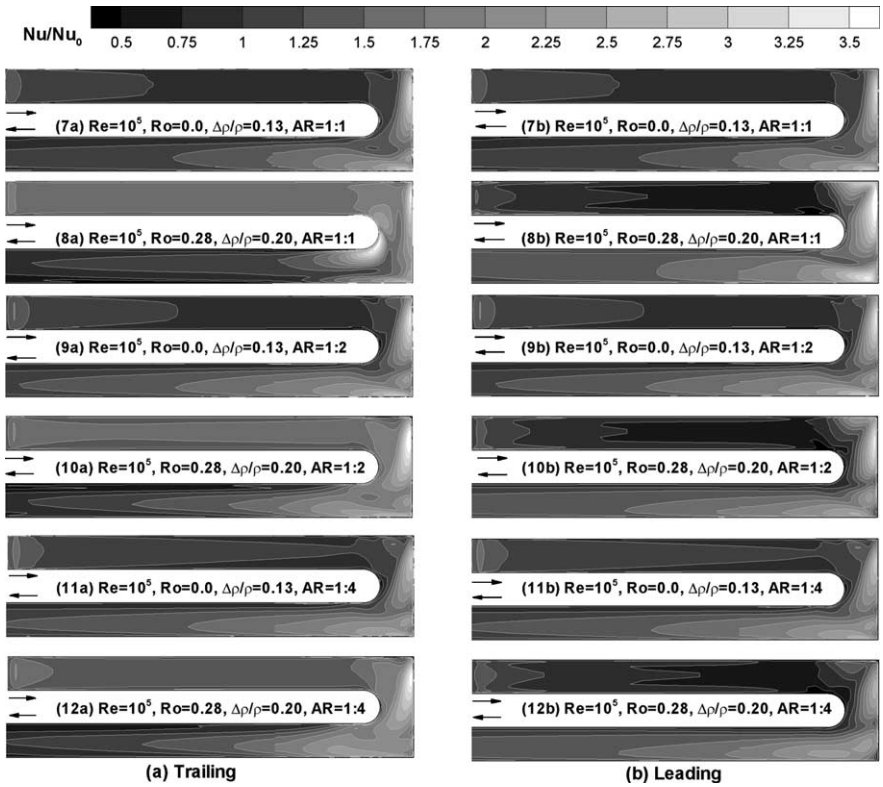

Fig. 10. Nusselt number ratio contours on (a) trailing and (b) leading surface for higher Reynolds number cases (Re = 100,000; Cases 7–12).

Fig. 10 shows the detailed Nusselt number ratio contours of the leading and trailing surfaces for high Reynolds number cases. When comparing to the low Reynolds number results shown in Fig. 7, it is clearly seen that the Nusselt number ratio decreases in both the non-rotating and rotating ducts when the Reynolds number is increased. In general, the Nusselt number ratios are high on the outer surface of the bend due to flow impingement. Another high heat transfer region was observed after the bend as the flow enters the second passage. For the non-rotating cases (Cases 7, 9 and 11), the effects of channel aspect ratios are relatively small and the Nusselt number ratio contours are very similar among three different aspect ratio ducts.

For the high Reynolds number and high rotation number conditions (Cases 8, 10 and 12), the effects of rotation lead to an increase of the heat transfer on the first pass trailing surface and a decrease of Nusselt number ratios on the first pass leading surface since the Coriolis force induced vortices push the cold fluid toward the trailing surface. The trend is reversed in the second passage as the Coriolis force acts in the opposite direction. Compared to the non-rotating ducts, the effects of channel aspect ratios are more significant in rotating ducts because the size and shape of the secondary flow vortices (see Fig. 6) are strongly affected by the channel cross-sectional geometry under rotating conditions.

Fig. 11 compares the numerically predicted spanwise-averaged Nusselt number ratio for the non-rotating conditions. It is seen that the AR = 1:2 rectangular duct has the highest Nusselt number ratio (Nu/Nu_0) at the turn region since the counter-rotating vortices are stronger than those observed in either the AR = 1:1 or 1:4 ducts. Near the exit, the Nusselt number ratios (Nu/Nu_0) for all three ducts approach nearly the same value. This confirmed the previous observation that the flow pattern and heat transfer characteristics are not widely different in non-rotating channels with different aspect ratios. It should be noted here, however, the actual heat transfer coefficient (h) is significantly higher for the square duct in comparison with the rectangular ducts since the square duct has the smallest hydraulic diameter and hence the highest mean velocity.

Fig. 11 also shows the spanwise-averaged Nusselt number ratios for the non-rotating duct at two different Reynolds numbers of 10,000 and 100,000 for three different aspect ratio channels. In general, the Nusselt number ratios Nu/Nu_0 on the four surfaces decrease as the Reynolds number increases. However, it should be note that Nu_0 increases rapidly (proportional to $Re^{0.8}$)

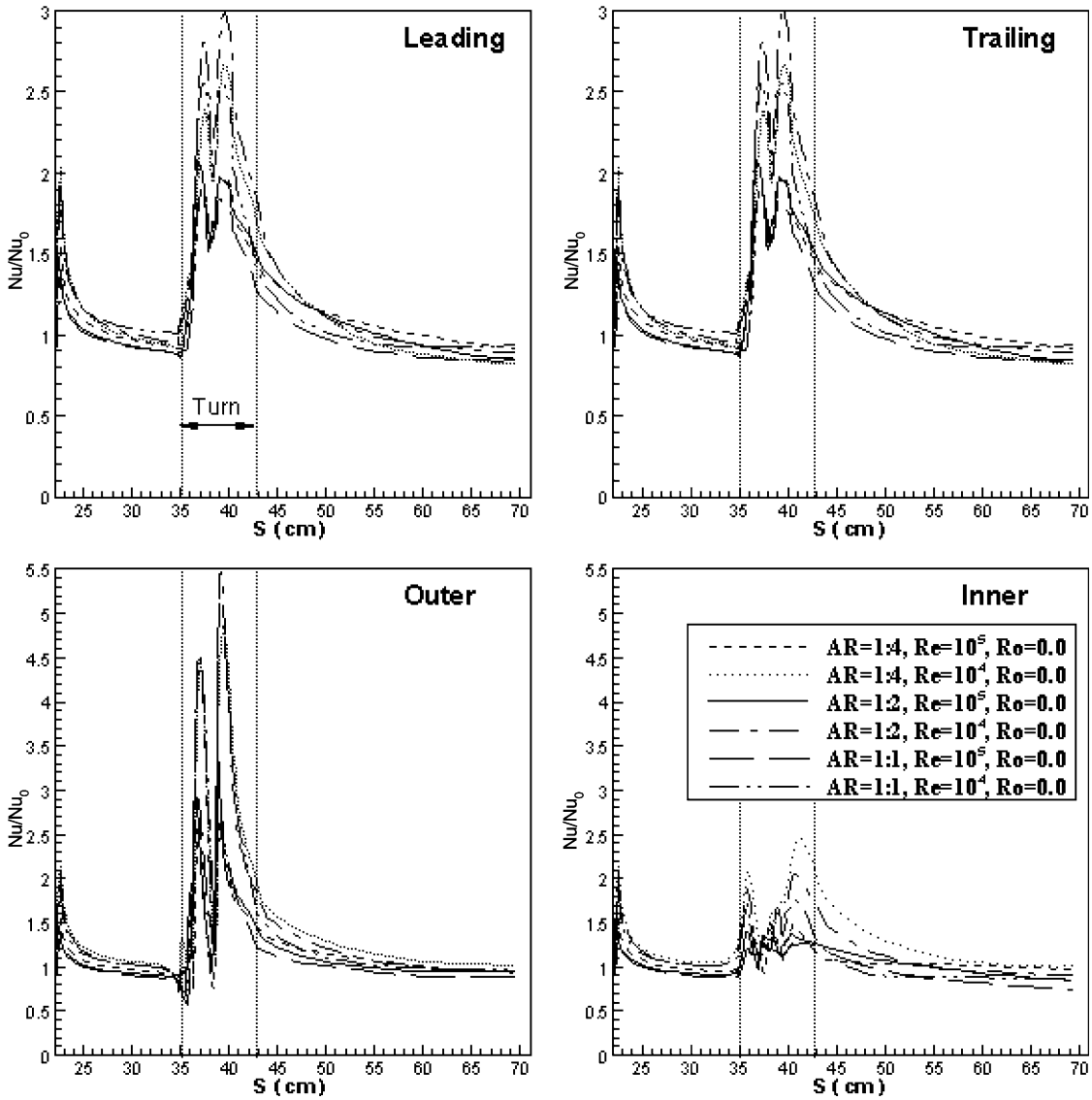

Fig. 11. Effect of Reynolds number on spanwise-averaged Nusselt number ratios for non-rotating ducts with aspect ratio of 1:1, 1:2 and 1:4 ($Ro = 0.0$, $\Delta\rho/\rho = 0.13$).

when the Reynolds number was increased from 10,000 to 100,000. Therefore, the actual heat transfer coefficients are still increase very significantly at $Re = 100{,}000$ even though the heat transfer enhancement decreases.

4.5. Effect of density ratio on heat transfer coefficient distribution

Fig. 12 shows the effect of inlet coolant-to-wall density ratio on the spanwise-averaged Nusselt number ratios for the rotating ducts with different aspect ratios. We will focus on the high Reynolds number ($Re = 100{,}000$) and high rotation number ($Ro = 0.28$) conditions with two different density ratios of 0.20 and 0.40. In the first passage of the square ducts (AR = 1:1), an increase in density ratio leads to a large increase of heat transfer on the trailing surface and a fairly significant decrease of Nusselt number ratios on the leading surface. However, the density ratio effect diminishes quickly in the low aspect ratio rectangular ducts of AR = 1:2 and 1:4. In the second passage, an increase in density ratio leads the Nusselt number ratios to decrease on both the leading and trailing surface. Near the exit, however, the effect of density ratio on Nusselt number ratio diminishes for the AR = 1:1 and 1:2 ducts.

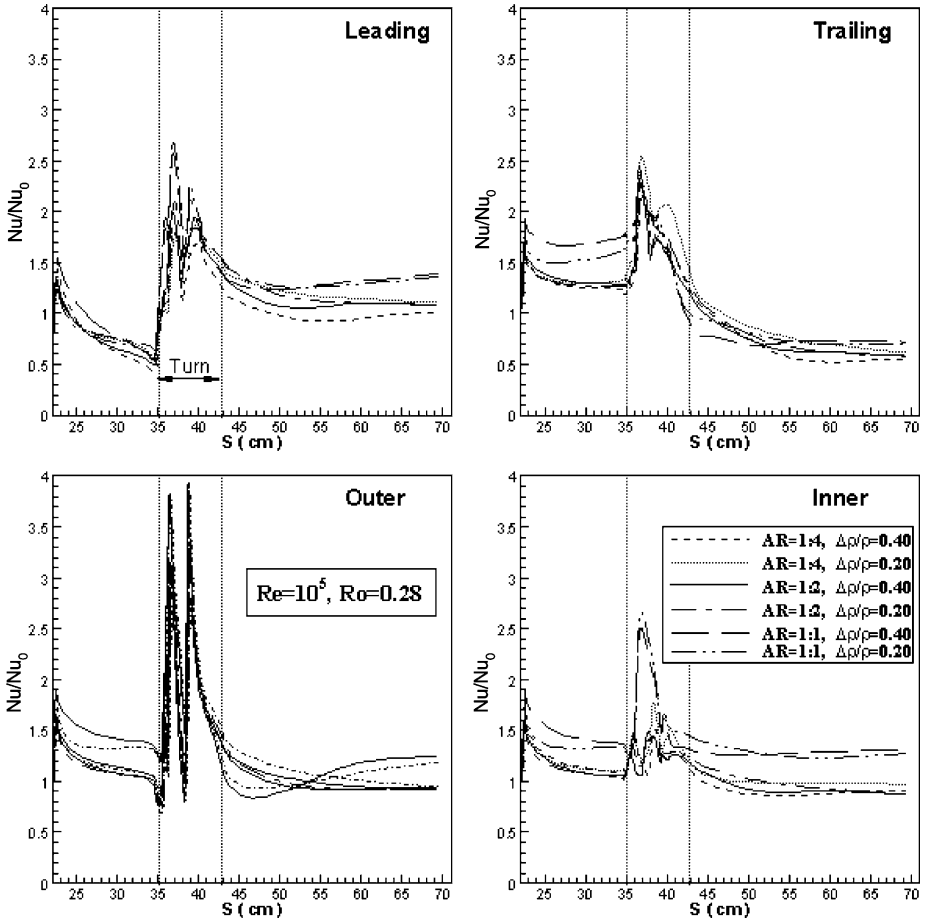

Fig. 12. Effect of density ratio on spanwise-averaged Nusselt number ratios for rotating ducts with aspect ratio of 1:1, 1:2 and 1:4 (Re = 100,000, Ro = 0.28).

4.6. Effect of aspect ratio and Reynolds number on spanwise averaged friction factor

Fig. 13 shows the spanwise-averaged friction factor ratio C_f/C_{f0} for the heated section of all three non-rotating channels for Re = 10,000 and 100,000. It is seen that the friction factors for the first passage maintain the fully developed values until a short distance ahead of the bend. Around the inner surface of the bend, the friction factor ratio increase sharply around the bend entrance due to local flow acceleration. Further downstream, the friction factor ratios drop sharply as the flow separates from the inner wall. The friction factor ratios fall below 1 in the separation region and increase again after the reattachment point. On the outer surface of the bend, the friction factor ratios drop significantly around the bend entrance due to the sudden expansion of the channel cross-section in the bend region. In the bend, the high momentum is pushed toward the outer surface by the centrifugal force induced by the streamline curvature. This leads to flow impingements on two different locations of the outer surface. The first impingement occurs just behind the shape corner of the first passage, while the second impingement occurs after the second shape corner near the entrance to the second passage. These flow impingements produced two sharp peaks in the bend region as seen in Fig. 13. It is further noted that the friction factor ratios also increase sharply along the leading and trailing surfaces of the bend. These increases are caused by the Coriolis force induced counter-rotating vortices (see Fig. 3) which enhance the mixing of high-momentum fluids in the core region with the low-momentum fluids in the near-wall region. After the bend, the friction factor ratios return gradually their fully developed values in the second passage. In general, the friction factor ratios are somewhat higher for rectangular ducts since the counter-rotating vortices were able to grow into circular shapes and reach full strength.

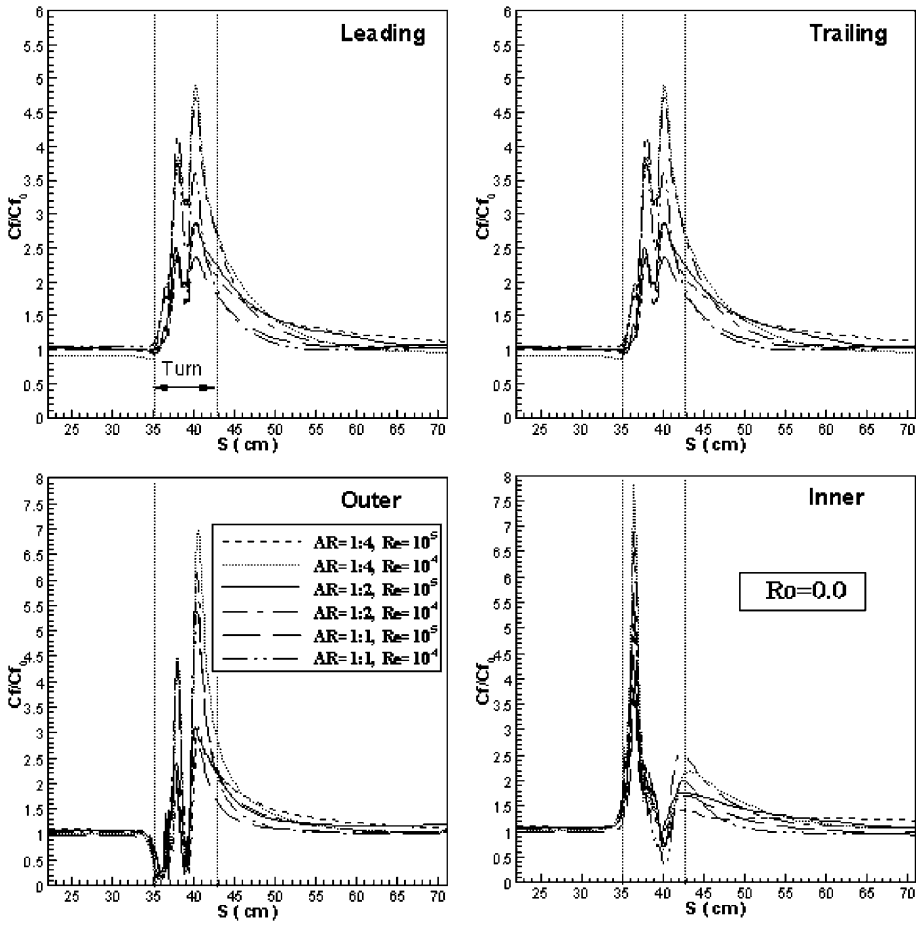

Fig. 13. Effect of Reynolds number on friction factor ratios in non-rotating ducts with aspect ratio of 1:1 and 1:2 and 1:4 ($Ro = 0.0$, $\Delta\rho/\rho = 0.13$).

Fig. 13 also shows the effect of the Reynolds number on the spanwise-averaged friction factor ratios for the non-rotating ducts with three different aspect ratios. In the first passage, the friction factor ratio changes only slightly when the Reynolds number was increased from 10,000 to 100,000. However, the actual friction factors are considerably lower for higher Reynolds number cases since C_{f0} is proportional to $Re^{-0.25}$. Around the bend region, the friction factor ratios at $Re = 100{,}000$ were about 40–50% lower than the corresponding values at $Re = 10{,}000$. After the bend, the friction factor ratios in all three ducts return gradually to about 1.0 for both the low and high Reynolds number flow conditions.

4.7. Effects of rotation on spanwise-averaged friction factor

Fig. 14 shows the spanwise-averaged friction factor ratio C_f/C_{f0} on the heated section of all three rotating channels with $Ro = 0.14$. In the first passage, the Coriolis force pushed the high-momentum fluid toward the trailing surface which creates a thinner boundary layer with increased friction factor ratios on the trailing surface. The same Coriolis force also caused the thickening of the boundary layer and a reduction of the friction factor ratios on the leading surface. In the bend region, the Nusselt number ratios increase on all four walls due to the mixing of high and low momentum fluids, the flow impingement on the outer surface, and the boundary layer flow reattachment on the inner surface. After the bend, the Coriolis force in the second passage acts in the opposite direction of that observed in the first passage. Consequently, the friction factor increases on the leading surface and decreases on the trailing surface as the fluid moves radially inward in the second passage. It is also observed that the effect of the channel aspect ratio on the friction factor is significant on the leading surfaces and side walls of the second passage of the rotating ducts.

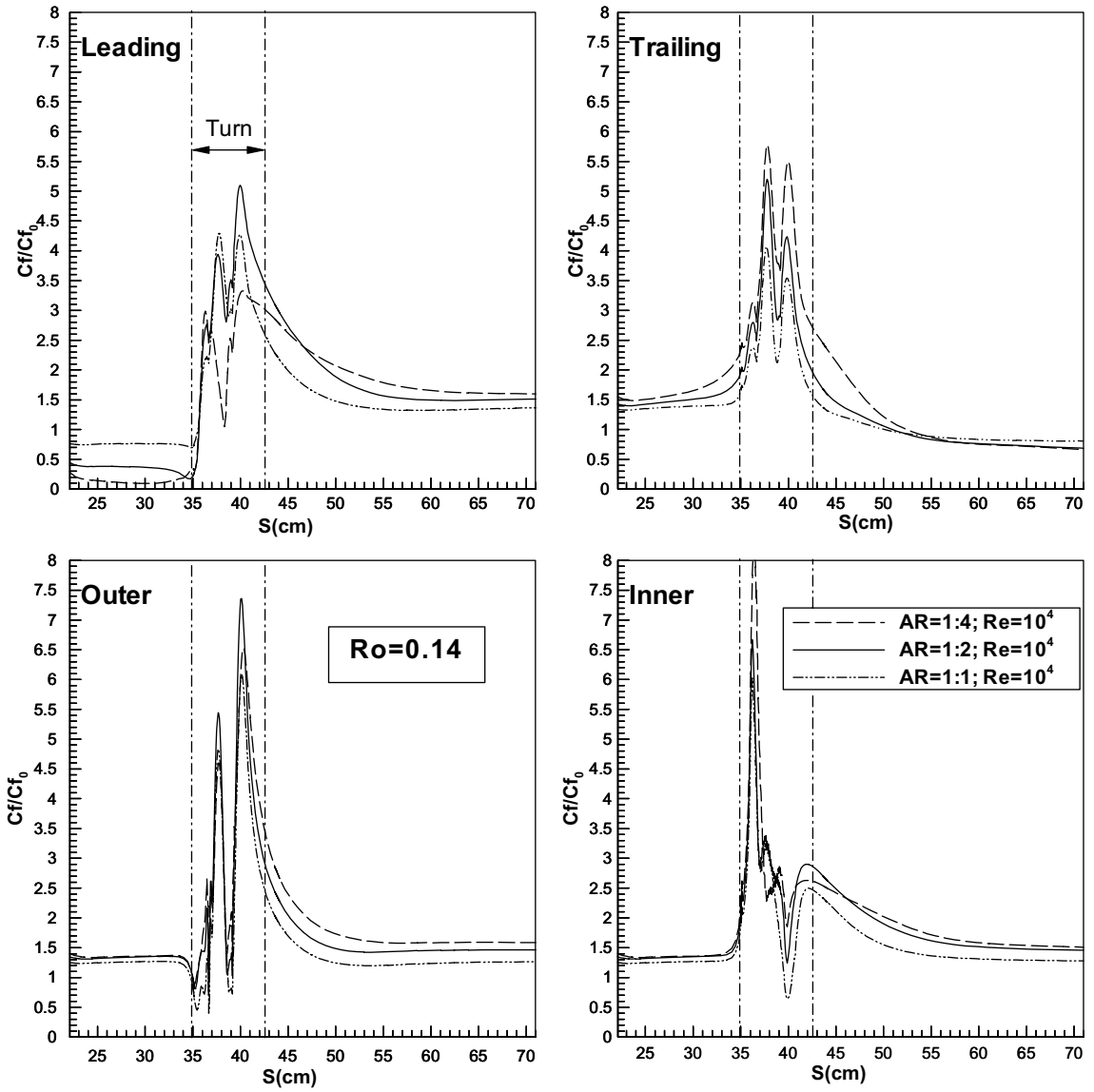

Fig. 14. Effect of rotation on friction factor ratios for rotating ducts with lower Reynolds number cases ($Ro = 0.14$, $Re = 10{,}000$, $\Delta\rho/\rho = 0.13$) (Cases 2, 4 and 6).

5. Conclusions

A multi-block RANS method was employed to predict three-dimensional flow and heat transfer in rotating and non-rotating ducts with three different aspect ratios of AR = 1:1, 1:2, and 1:4. It predicted fairly well the complex three-dimensional flow and heat transfer characteristics in the low aspect ratio rectangular channels with rotation and centrifugal buoyancy forces. Primary findings from this study are summarized as follows:

1. For non-rotating ducts, a pair of symmetric counter-rotating vortices was generated in the bend region. The highest heat transfer enhancement was observed in AR = 1:2 duct when the counter-rotating vortices grow to full strength and occupy the entire channel. As the aspect ratio reduces to AR = 1:4, the vortices and the heat transfer enhancements are confined to the leading and trailing surfaces.
2. For all three rotating ducts at $\beta = 90°$ channel orientation, the Coriolis force produce a pair of counter-rotating vortices perpendicular to the bend-induced

vortices. The combined effects of rotation and turn lead to the growth of the vortex near the leading surface. The leading surface vortex continue to expand in the vertical direction as the channel aspect ratio was reduced from AR = 1:1 to 1:4.

3. For all three different aspect ratio ducts, the Nusselt number ratios decrease with increasing Reynolds numbers. The friction factor ratios also decrease when the Reynolds number was increased from 10,000 to 100,000.
4. For non-rotating ducts, the channel aspect ratio has a small effect on spanwise-averaged Nusselt number ratio and friction factor ratio except for the turn region.
5. The channel rotation leads to higher heat transfer on first pass trailing surface and lower heat transfer on first pass trailing surface. This trend is reversed in the second pass. The effects of rotation on Nusselt number ratio become much more pronounced for low aspect ratio (AR = 1:2 and 1:4) rectangular channels.

Acknowledgments

This publication was prepared with the support of the US Department of Energy, Office of Fossil Energy, and National Energy Technology Laboratory. However, any opinions, findings, conclusions, or recommendations expressed herein are those of the authors and do not necessarily reflect the views of the DOE. The computations were performed on the SGI Origin 3800 at the Texas A&M Supercomputer Center under a supercomputer research grant. The support of all of the above institutions is greatly appreciated.

References

[1] C. Prakash, R. Zerkle, Prediction of turbulent flow and heat transfer in a ribbed rectangular duct with and without rotation, ASME J. Turbomach. 177 (1995) 255–264.
[2] T. Bo, H. Iacovides, B.E. Launder, Developing buoyancy-modified turbulent flow in ducts rotating in orthogonal mode, ASME J. Turbomach. 117 (3) (1995) 474–484.
[3] D.L. Besserman, S. Tanrikut, Comparison of heat transfer measurements with computations for turbulent flow around a 180-deg degree bend, Paper 91-GT-2, ASME, 1991.
[4] P.S. Sathyamurthy, K.C. Karki, S.V. Patankar, Prediction of turbulent flow and heat transfer in a rotating square duct with a 180 degree bend, Paper 94-GT-197, 1994.
[5] D.M. McGrath, D.G.N. Tse, A combined experimental/computational study of flow in turbine blade cooling passage. Part 2. Numerical simulations, Paper 95-GT-149, ASME, 1995.
[6] J.-J. Hwang, W.-J. Wang, D.-Y. Lai, Numerical simulation of turbulent heat transfer and flow in a rotating multiple-pass square channel, ASME 97-GT-367, 1997.
[7] J.H. Wagner, B.V. Johnson, F.C. Kopper, Heat transfer in rotating serpentine passage with smooth walls, ASME J. Turbomach. 113 (3) (1991) 321–330.
[8] H. Iacovides, B.E. Launder, H.Y. Li, The computation of flow development through stationary and rotating U-ducts of strong curvature, Int. J. Heat Fluid Flow 17 (1) (1996) 22–33.
[9] S.C. Cheah, H. Iacovides, B.E. Launder, LDA investigation of flow developing through rotating U-ducts, ASME Paper 94-GT-226, 1994.
[10] B. Bonhoff, U. Tomm, B.V. Johnson, I. Jennions, Heat transfer predictions for rotating U-Shaped coolant channels with skewed ribs and with smooth walls, ASME Paper 97-GT-162, 1997.
[11] M.A. Stephens, T.I.P. Shih, K.C. Civinskas, Computations of flow and heat transfer in a rotating U-shaped square duct with smooth walls, Paper No. 96-3161, AIAA, 1996.
[12] M.A. Stephens, T.I.P. Shih, Flow and heat transfer in a smooth U-duct with and without rotations, AIAA J. Propul. Power 15 (2) (1999) 272–279.
[13] Y.-L. Lin, T.I.-P. Shih, M.A. Stephens, M.K. Chyu, A numerical study of flow and heat transfer in a smooth and a ribbed U-duct with and without rotation, ASME J. Heat Transfer 123 (2001) 219–232.
[14] H.C. Chen, Y.J. Jang, J.C. Han, Computation of heat transfer in rotating two-pass square channels by a second-moment closure model, Int. J. Heat Mass Transfer 43 (9) (2000) 1603–1616.
[15] H.C. Chen, Y.J. Jang, J.C. Han, Near-wall second-moment closure for rotating multi-pass cooling channels, J. Thermophys. Heat Transfer 14 (2) (2000) 201–209.
[16] Y.J. Jang, H.C. Chen, J.C. Han, Computation of flow and heat transfer in two-pass channels with 60° ribs, ASME J. Heat Transfer 123 (3) (2001) 563–575.
[17] Y.J. Jang, H.C. Chen, J.C. Han, Numerical prediction of the flow and heat transfer in a two-pass square duct with 90° ribs, Int. J. Rotating Machinery 7 (3) (2001) 195–208.
[18] S.V. Ekkad, J.C. Han, Detailed heat transfer distributions in two-pass square channels with rib turbulators, Int. J. Heat Mass Transfer 40 (11) (1997) 2525–2537.
[19] Y.J. Jang, H.C. Chen, J.C. Han, Flow and heat transfer in a rotating square channel with 45-deg angled ribs by Reynolds stress turbulence model, ASME J. Turbomach. 123 (1) (2001) 124–132.
[20] B.V. Johnson, J.H. Wagner, G.D. Steuber, F.C. Yeh, Heat transfer in rotating serpentine passage with trips skewed to the flow, ASME J. Turbomach. 116 (1994) 113–123.
[21] Al.-M. Qahtani, Y.J. Jang, H.C. Chen, J.C. Han, Prediction of flow and heat transfer in rotating two-pass rectangular channels with 45-deg rib turbulators, J. Turbomach. 124 (2002) 242–250.
[22] G. Su, S. Teng, H.C. Chen, J.C. Han, Computation of flow and heat transfer in rotating rectangular channels (AR = 4) with V-shaped ribs by a Reynolds stress turbulence model, ASME Paper GT2003-38348, 2003.

[23] G.M.S. Azad, M.J. Uddin, J.C. Han, H.K. Moon, B. Glezer, Heat transfer in two-pass rectangular rotating channels with 45-deg parallel and crossed rib turbulators, J. Turbomach. 124 (2001) 251–259.

[24] E. Lee, L.M. Wright, J.C. Han, Heat transfer in rotating rectangular channels (AR = 4:1) with V-shaped and angled rib turbulators with and without gaps, ASME Paper Number GT-2003-38900, 2003.

[25] W.L. Fu, L. Wright, J.C. Han, Heat transfer in two-pass rotating rectangular channels (AR = 1:2 and AR = 1:4) with 45° angled rib turbulators, ASME Paper GT2004-53261.